Machine learning-accelerated computational non-equilibrium flow: Deep neural network prediction of transport properties

Yaowen Du(杜耀文)[1], Surong Sun(孙素蓉)[1,†], Haixing Wang(王海兴)[1,‡], Zhenwei Shi(史振威)[1], Heji Huang(黄河激)[2], Cong Yan(闫聪)[2], Xian Meng(孟显)[2], and Xuan Chen(陈轩)[3]

[1] *School of Astronautics, Beihang University, Beijing* 102206, *China*
[2] *Institute of Mechanics, Chinese Academy of Sciences, Beijing* 100190, *China*
[3] *Science and Technology on Space Physics Laboratory, Beijing* 100076, *China*

(Received 11 September 2025; revised manuscript received 6 November 2025; accepted manuscript online 19 November 2025)

The characterization of non-equilibrium transport phenomena plays an essential role in modeling many fluid flow processes, such as high-speed shocks, flame propagation, and plasma flow. The Boltzmann perturbation method, originating from microscopic particle collisions, effectively captures transport properties within fluids. However, under non-equilibrium conditions, the computational cost of coupling iterative solvers for transport properties in computational fluid dynamics becomes prohibitively high, leading to an unfavorable trade-off between accuracy and tractability. To overcome this challenge, we employ a deep neural network in this work to replace the Boltzmann perturbation method for obtaining transport properties in high-speed air non-equilibrium flows, enabling accelerated computations for non-equilibrium flow. For simulating non-equilibrium airflow around hypersonic vehicles, our method achieves comparable accuracy to the Boltzmann perturbation method, with average errors in transport properties below 0.5%. Compared to the conventional iterative coupling approach, the deep neural network eliminates the need for solving collision parameters between particles and Sonine polynomials, resulting in a 50- to 70-fold computational speedup. Furthermore, the neural network demonstrates excellent generalization capabilities for other flight geometries and conditions. Our approach exemplifies how computational fluid dynamics can leverage machine learning from the perspective of fluid physical properties to improve simulations.

Keywords: plasma properties, nonequilibrium gas dynamics, machine learning

PACS: 52.25.–b, 47.70.Nd

DOI: 10.1088/1674-1056/ae2112 **CSTR:** 32038.14.CPB.ae2112

CPB Online In Press

1. Introduction

The numerical simulation of complex flow fields, such as high-speed vehicle flow, combustion dynamics evolution, and plasma flow development, requires the calculation of transport properties such as viscosity coefficients, thermal conductivity, and diffusion coefficients.[1–4] The Boltzmann perturbation method developed by Chapman and Enskog represents the state-of-the-art approach for computing these transport properties.[5] However, for the simulations of those complex flows involving non-equilibrium conditions and large parameter gradients, it is necessary to first solve for collision parameters between different particles (from interaction potentials to collision cross-sections and collision integrals) based on temperature and species information within the flow field, and then to solve Sonine polynomials to obtain diffusion coefficients characterizing mass transport, viscosity coefficients representing momentum transport, and thermal conductivity describing energy transport.[6] Due to the mutual influence between the transport properties and the flow field parameters, iterative calculations between flow field solutions and the Boltzmann perturbation method are required, a process that incurs significant computational costs. For decades, this challenge has created a detrimental trade-off between accuracy and usability in non-equilibrium flow simulations.[7–9]

Taking the calculation of transport properties in high-speed air flows as an example, the high computational cost required for precise determination of transport coefficients has driven the development of approximate transport property models for high-speed computational fluid dynamics (CFD), such as the widely used Wilke/Blottner/Eucken and Gupta–Yos/CCS models.[10–13] The Wilke/Blottner/Eucken model is simpler, relying on predefined viscosity or thermal conductivity curve fits as temperature-dependent functions for each chemical species considered in the flow. The Gupta–Yos/CCS model depends on collision cross-section curve databases fitted as temperature functions for every possible binary interaction. Consequently, only the latter accounts for the nature of interactions between different particles. Global mixture coefficients are then calculated using properties determined per species or per collision pair through the application of approximate mixing rules. These approximate models exhibit

†Corresponding author. E-mail: ssr18@buaa.edu.cn
‡Corresponding author. E-mail: whx@buaa.edu.cn

© 2026 Chinese Physical Society and IOP Publishing Ltd. All rights, including for text and data mining, AI training, and similar technologies, are reserved.

rapidly increasing computational losses relative to precise formulations under non-equilibrium, extreme high-temperature conditions (where substantial ionized products exist), ultimately leading to a decline in the prediction accuracy of flow parameters.[5,14]

To address this, we introduce a deep learning method for calculating transport properties, aiming to achieve high-fidelity and computationally efficient transport property computation in non-equilibrium complex flow simulations. A deep neural network (DNN) is trained on manifold-sampled data from non-equilibrium flow simulations across a wide range of conditions. Leveraging the high-dimensional nonlinear function approximation capability of DNNs, these networks enable rapid and accurate computation of non-equilibrium transport properties. The DNN simplifies the intricate collision parameters and polynomial calculations involved in the Boltzmann perturbation method into a series of matrix multiplications. Furthermore, by coupling with the non-equilibrium flow solver, the DNN is integrated into the flow field calculation, achieving a 50- to 70-fold improvement in computational efficiency.

The paper is organized as follows: first, the structure of the DNN and its training methodology are presented, and the coupling process between the DNN and the non-equilibrium flow-field calculation is given. Second, the computational accuracy of the DNN is verified through *a priori* method, and its efficiency and accuracy in predicting the non-equilibrium transport properties are further evaluated in conjunction with the flow-field coupling analysis. Furthermore, generalization calculations are conducted under more shapes and flight conditions. Finally, the conclusions are drawn.

2. Methodology

Figure 1 illustrates the flowcharts of the conventional non-equilibrium flow field–Chapman Enskog coupling calculation method (NeFlow-CE) and the non-equilibrium flow field-DNN coupling acceleration method (NeFlow-DNN) proposed in this study. For the conventional calculation method, based on the non-equilibrium temperatures and species concentrations within the flow field, the process computes interaction potential functions for different particle pairs, then calculates collision parameters (collision integrals, cross-sections), and ultimately derives transport properties through Sonine polynomial expansions before feeding them back into the flow governing equations. There is a strong interdependent effect and coupling relationship between the temperatures, component parameters, and transport properties within the flow field, necessitating complex iterative solutions between them. In contrast, the flow field-DNN coupling acceleration method streamlines these complex microscopic collision parameters and polynomial-solving procedures into a neural network-based matrix computation framework. The remainder of this section details the implementation methodology for the non-equilibrium flow field solver, the Boltzmann perturbation method, and the DNN.

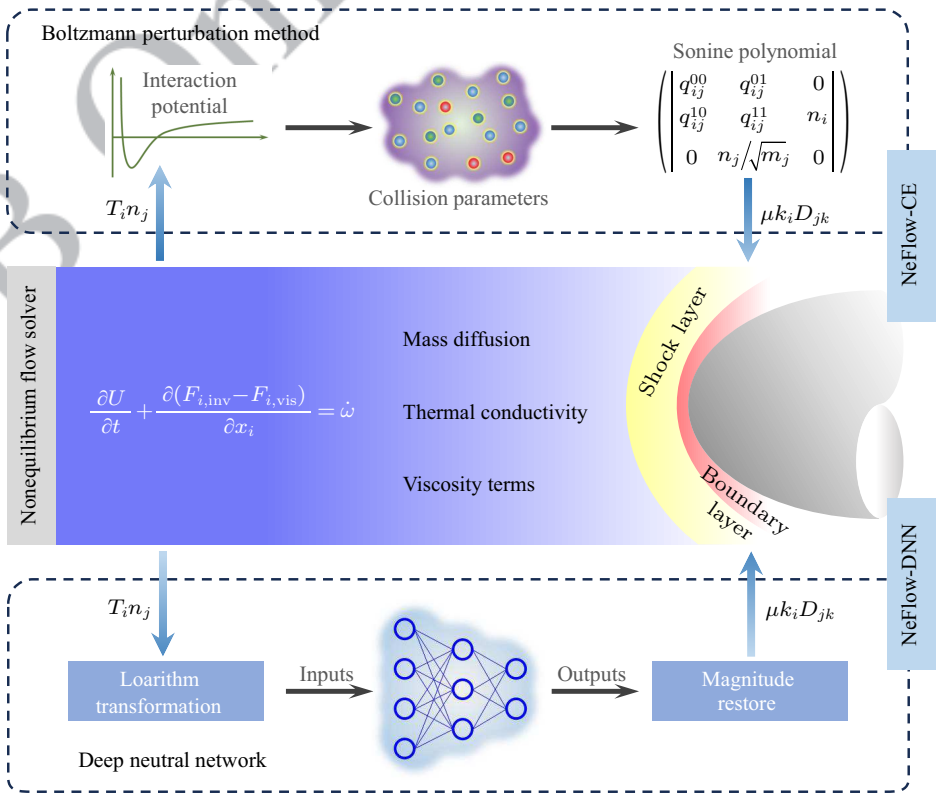


Fig. 1. Schematic diagram of the flowcharts of the conventional NeFlow-CE method and the NeFlow-DNN acceleration method.

CPB Online In Press

2.1. Non-equilibrium flow solver

In the non-equilibrium flow simulation, the two-temperature chemical non-equilibrium flow governing equations are employed to simulate the high-speed, high-enthalpy flow around a blunt cone ELECTRE. The flow is assumed to be laminar, continuous, and axisymmetric. The heavy-species temperature and electron temperature are respectively assumed to satisfy the Maxwellian distribution, and are solved by two separate energy equations. The air mixture is assumed to consist of nine species: N_2, O_2, NO, N, O, N^+, O^+, NO^+, and e^-. Detailed chemical reaction processes are described in Ref. [15].

The governing equations consist of the continuity equation, species conservation equations, momentum equations, total energy equation, and electron energy equation, which are written as follows:

$$\frac{\partial \rho}{\partial t}+\frac{\partial(\rho u)}{\partial z}+\frac{\partial(\rho v)}{\partial r}+\frac{\rho v}{r}=0, \tag{1}$$

$$\frac{\partial(\rho f_i)}{\partial t}+\frac{\partial(\rho f_i u)}{\partial z}+\frac{\partial(\rho f_i v)}{\partial r}+\frac{\rho f_i v}{r} = -\frac{\partial J_{iz}}{\partial z}-\frac{\partial J_{ir}}{\partial r}-\frac{J_{ir}}{r}+\dot{n}_i m_i, \tag{2}$$

$$\frac{\partial(\rho u)}{\partial t}+\frac{\partial(\rho uu+p)}{\partial z}+\frac{\partial(\rho uv)}{\partial r}+\frac{\rho uv}{r} = \frac{\partial \tau_{zz}}{\partial z}+\frac{\partial \tau_{rz}}{\partial r}+\frac{\tau_{rz}}{r}, \tag{3}$$

$$\frac{\partial(\rho v)}{\partial t}+\frac{\partial(\rho uv)}{\partial z}+\frac{\partial(\rho vv+p)}{\partial r}+\frac{\rho vv+p}{r} = \frac{\partial \tau_{zr}}{\partial z}+\frac{\partial \tau_{rr}}{\partial r}+\frac{\tau_{rr}-\tau_{\theta\theta}}{r}, \tag{4}$$

$$\frac{\partial(\rho e_t)}{\partial t}+\frac{\partial[(\rho e_t+p)u]}{\partial z}+\frac{\partial[(\rho e_t+p)v]}{\partial r}+\frac{(\rho e_t+p)v}{r} = \frac{\partial\left(u\tau_{zz}+v\tau_{zr}-q_z-\sum_i h_i J_{iz}\right)}{\partial z}+\frac{\partial\left(u\tau_{rz}+v\tau_{rr}-q_r-\sum_i h_i J_{ir}\right)}{\partial r}+\frac{u\tau_{rz}+v\tau_{rr}-q_r-\sum_i h_i J_{ir}}{r}-E_c, \tag{5}$$

$$\frac{\partial(\rho_e e_e)}{\partial t}+\frac{\partial[(\rho_e e_e+p_e)u]}{\partial z}+\frac{\partial[(\rho_e e_e+p_e)v]}{\partial r}+\frac{(\rho_e e_e+p_e)v}{r} = \frac{\partial(-q_{ez}-h_e J_{ez})}{\partial z}+\frac{\partial(-q_{er}-h_e J_{er})}{\partial r}+\frac{-q_{er}-h_e J_{er}}{r}-E_{ce}+Q_{elas}, \tag{6}$$

where u, v, ρ, f_i, h_i, p, e_t, and e_e represent the axial velocity, radial velocity, gas density, mass fraction of species i, specific enthalpy of species i, gas pressure, total specific energy, and electron internal energy, respectively. E_c and E_{ce} are respectively the chemical reaction energy sources for total energy and electron energy. Q_{elas} indicates the energy source caused by elastic collisions between the electrons and heavy species.

In the above governing equations, the terms used to describe mass, momentum, and energy transport include the following expressions.

(i) Mass diffusion flux J_i is obtained by the self-consistent effective binary diffusion coefficient,[16] and expressed as

$$J_i=-\left(\frac{pm_iD_i}{RT_i}\right)G_i+y_i\sum_j\left(\frac{pm_jD_j}{RT_j}\right)G_j, \tag{7}$$

where D_i is the effective diffusion coefficient, and G_i is the diffusion driving force of species i due to the gradients of concentration, pressure, and temperature, and is expressed as

$$G_i=\nabla\left(\frac{p_i}{p}\right)+\left(\frac{p_i}{p}-\frac{\rho_i}{\rho}\right)\nabla\ln p -\frac{1}{p}\sum_j(\beta_{ij}\nabla\ln T_j-\beta_{ji}\nabla\ln T_i), \tag{8}$$

where β_{ij} is the thermal diffusion coefficient.

(ii) The shear stress tensor τ is written as

$$\begin{aligned}\tau_{rr}&=2\mu\frac{\partial v}{\partial r}-\frac{2}{3}\mu\left(\frac{1}{r}\frac{\partial(rv)}{r}+\frac{\partial u}{\partial z}\right),\\ \tau_{\theta\theta}&=2\mu\frac{v}{r}-\frac{2}{3}\mu\left(\frac{1}{r}\frac{\partial(rv)}{r}+\frac{\partial u}{\partial z}\right),\\ \tau_{zz}&=2\mu\frac{\partial u}{\partial z}-\frac{2}{3}\mu\left(\frac{1}{r}\frac{\partial(rv)}{r}+\frac{\partial u}{\partial z}\right),\\ \tau_{rz}&=\tau_{zr}=\mu\left(\frac{\partial v}{\partial z}+\frac{\partial u}{\partial r}\right),\end{aligned} \tag{9}$$

where μ is the viscosity coefficient of the gas.

(iii) Heat conduction vectors are given by

$$\begin{aligned}q&=-k_h\nabla T_h-k_e\nabla T_e,\\ q_e&=-k_e\nabla T_e,\end{aligned} \tag{10}$$

where k_h and k_e are the thermal conductivities of heavy species and electrons, respectively.

Apparently, to ensure precise computation of these transport terms, it is essential to determine reliable and accurate transport coefficients, including diffusion coefficients, viscosity coefficients, and thermal conductivities.

2.2. The perturbative Chapman–Enskog method

Calculation of the non-equilibrium transport properties is carried out through the approximate solution of Boltzmann's equation using the first-order perturbation technique proposed by Chapman and Enskog.[6] This method assumes that the particle distribution function is a first-order perturbation to the Maxwellian distribution, and the perturbation is then expressed in a series of Sonine polynomials, finally leading to a system of linear equations that can be suitably solved to obtain different transport properties.

CPB Online In-Press

The transport coefficients can be expressed as linear combinations of a set of collision integrals, $\Omega_{ij}^{(l,s)}$, defined as

$$\Omega_{ij}^{(l,s)} = \sqrt{2\pi k_{\mathrm{B}} T_{ij}^{*}/m_{ij}^{*}} \int_0^{\infty}\int_0^{\infty} \exp(-\gamma_{ij}^{2})\gamma_{ij}^{2s+3} \times (1-\cos^{l}\chi) b\,\mathrm{d}b\cdot \mathrm{d}\gamma_{ij}, \tag{11}$$

where k_{B} is the Boltzmann constant, m_{ij}^{*} and T_{ij}^{*} are respectively the effective mass and the effective temperature of the colliding particles. χ is the deflection angle, b is the impact parameter, and γ_{ij} is the impact reduced energy. The l in the superscript represents the type of collision integral, where $l=1$ and $l=2$ respectively denote the diffusion collision integral and the viscous collision integral, and s indicates different orders of the same type of collision integral. In this paper, the Lennard–Jones potential, exponential repulsive potential, and Morse potential are adopted for the calculation of collision integrals between the neutral particles. The charged–neutral collision integrals are obtained by the Morse potential, repulsive potential, and polarizability model. The shielded Coulomb potential is used for determining these collision integrals between the charged particles.[17]

(I) Viscosity

The calculation of the viscosity coefficient of high-temperature air takes into account the influence of collisions between heavy particles and neglects the collision effect of electrons with relatively small mass. The viscosity coefficient is calculated using the first-order approximation expansion of the Sonine polynomial:

$$\mu = -\frac{5\sqrt{2\pi k_{\mathrm{B}} T_{\mathrm{h}}}}{2\left|Q_{ij}^{00}\right|}\begin{vmatrix} Q_{ij}^{00} & n_j\sqrt{m_j} \\ n_j & 0 \end{vmatrix}, \tag{12}$$

where Q_{ij}^{00} is an $i\times j$-order matrix. The matrix expression in the formula refers to Ref. [17].

(II) Diffusion coefficients

The binary diffusion coefficient D_{ij}^{b} between components i and j is calculated using the first-order approximation formula

$$D_{ij}^{b} = \left(\frac{2\pi k_{\mathrm{B}}}{m_{ij}^{*}T_{ij}^{*}}\right)^{1/2}\frac{3T_i}{16n\bar{\Omega}_{ij}^{(1,1)}}. \tag{13}$$

(III) Thermal conductivity

According to the different collisional particles that cause energy transport, the thermal conductivity k can be classified into the thermal conductivity of heavy particles k_{h} and the thermal conductivity of electrons k_{e}. According to the different types of transported energy, k_{h} can be further divided into the translational thermal conductivity $k_{\mathrm{tr,h}}$ and the internal thermal conductivity k_{int}.

The $k_{\mathrm{tr,h}}$ is expressed in the form of the second-order expansion of the Sonine polynomial:

$$k_{\mathrm{tr,h}} = -\frac{75k_{\mathrm{B}}}{8}\frac{\sqrt{2\pi k_{\mathrm{B}}T_{\mathrm{tr}}}}{|q|}\left(\begin{vmatrix} q_{ij}^{00} & q_{ij}^{01} & 0 \\ q_{ij}^{10} & q_{ij}^{11} & n_i \\ 0 & n_j/\sqrt{m_j} & 0 \end{vmatrix}\right). \tag{14}$$

The q_{ij}^{mp} elements are computed as in Ref. [17].

The internal thermal conductivity of heavy particles is due to the existence of internal degrees of freedom such as rotation, vibration, and electron excitation within the particles. In this paper, the internal thermal conductivity of particles is calculated by using the Eucken approximation

$$k_{\mathrm{int}} = \sum_{i\neq e} pD_{ii}/RT_{\mathrm{h}}C_{p,ve}^{i}\cdot\left(\sum_{j\neq e}\frac{x_j}{x_i}\frac{D_{ii}}{D_{ij}}\right)^{-1}. \tag{15}$$

In the formula, $C_{p,i}$ is the specific heat at constant pressure of the i-th species. D_{ii} and D_{ij} respectively represent the self-diffusion coefficient of component i and the binary diffusion coefficient between components i and j. R is the universal gas constant, and x_i is the mole fraction of component i.

The k_{e} is expressed in the form of a third-order expansion

$$k_{\mathrm{e}} = \frac{75n_{\mathrm{e}}^{2}k_{\mathrm{B}}}{8}\left(\frac{2\pi k_{\mathrm{B}}T_{\mathrm{e}}}{m_{\mathrm{e}}}\right)^{1/2}\left(q^{11}-\frac{\left(q^{12}\right)^{2}}{q^{22}}\right)^{-1}, \tag{16}$$

where q^{mp} elements are computed from associated collision integrals as in Ref. [18].

Figure 2 compares the transport properties calculated using the present Boltzmann perturbation method with those from conventional approximate models (including the widely used Wilke/Blottner/Eucken and Gupta–Yos/CCS models) under the condition of chemical equilibrium air at 1 atm pressure across a temperature range of 300 K to 2×10^{4} K. From Fig. 2(a), it can be observed that when ionization reactions become significant, conventional approximate models exhibit severe deviations in the calculated viscosity coefficient. At approximately 8000 K, the deviation of the Gupta–Yos/CCS model relative to the Boltzmann perturbation method is within 10%. This deviation persists until the viscosity peak at 10^{4} K, with the difference reaching as high as 50% at 1.4×10^{4} K. Typically, this method overestimates the viscosity coefficient. The Wilke/Blottner/Eucken model shows greater sensitivity to ionization at high temperature, exhibiting a deviation greater than 10% at 8000 K. By 1.2×10^{4} K, the viscosity coefficient is underestimated with a deviation of 75%. Similarly, approximate models display even more significant deviations in the calculation of frozen thermal conductivity at high temperature. The substantial difference in the solution behavior of the Wilke/Blottner/Eucken model at high temperatures is primarily due to its failure to account for electron–heavy particle interactions, which become prominent contributors at high temperature conditions. The solution error in the Gupta–Yos/CCS model arises from two aspects: first, its reliance on the first-order approximation Chapman–Enskog theory; second, due to inadequate collision cross-sections at high temperature.

CPB Online In Press

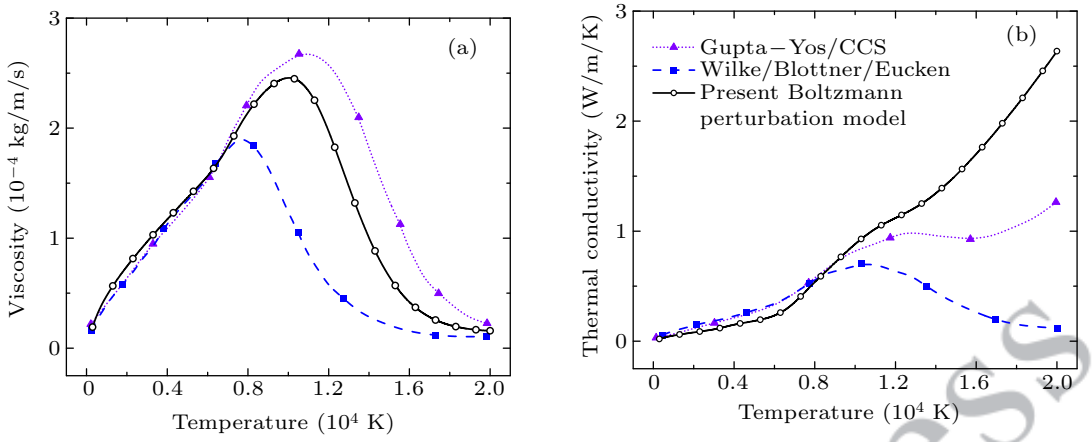


Fig. 2. Comparisons of three methods for (a) viscosity coefficient and (b) frozen thermal conductivity of equilibrium air at 1 atm. The unit 1 atm = 1.101325×10^5 Pa.

2.3. Deep neural network

The Boltzmann perturbation method involves extensive calculation of collision parameters and polynomial solving, resulting in low efficiency in fluid numerical simulations. To this end, this paper constructs a DNN to achieve rapid prediction of transport properties and acceleration of CFD. Figure 3 presents a schematic diagram of the construction and training process of the DNN, including: sample generation, data preprocessing, and DNN construction.

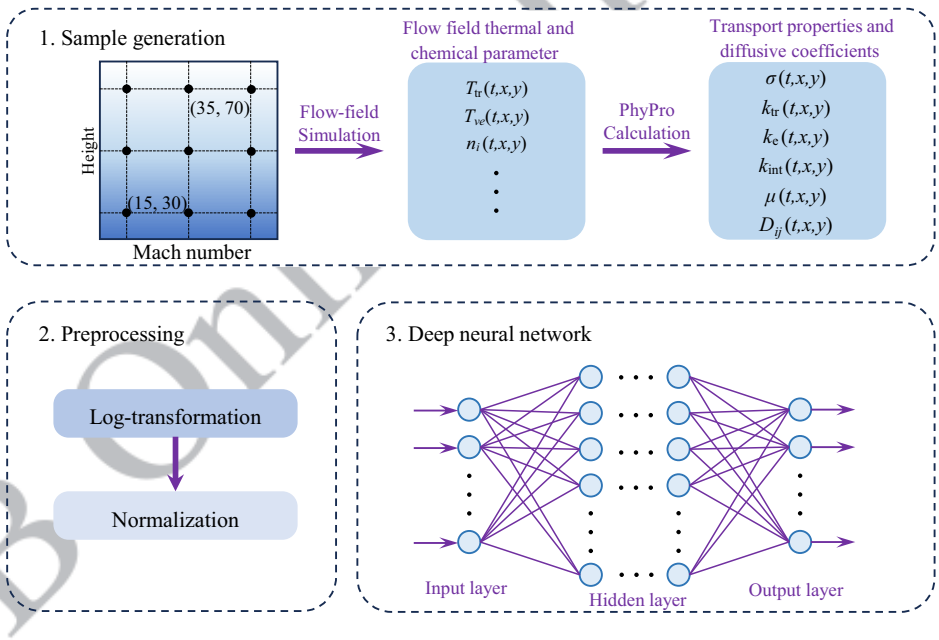


Fig. 3. Schematic diagram of the construction and training process of DNN.

(i) Manifold data sampling

The calculation of non-equilibrium transport properties is a typical high-dimensional dependency problem. In such cases, conventional high-dimensional sampling methods or Monte Carlo sampling would generate a large number of samples that deviate from real scenarios or are meaningless, thereby compromising the prediction performance of the DNN. To address this, the manifold sampling approach is adopted to construct the dataset for non-equilibrium transport properties. By performing non-equilibrium flow simulations under a wide range of altitude and velocity conditions, a sample dataset with universality and aligning with the distribution of real flow parameters is generated. This methodology effectively avoids invalid noise and the "curse of dimensionality" inherent in conventional high-dimensional sampling methods.

In order to ensure that the sample data can cover most of the non-equilibrium flow conditions as much as possible, in this paper, nine typical operating conditions are selected within the Mach number range of 10–40 and the flight altitude range of 20 km–80 km for transient flow field calculations. The flow field parameters at different times are obtained as input conditions, and the transport properties under these

CPB Online First Press

conditions are obtained through the perturbative Chapman–Enskog method. Finally, we obtain a sampling data set containing 918230 groups of data.

(ii) Data preprocessing

Since the number densities of chemical components, transport coefficients, and diffusion coefficients in the data involve cross-scale variations of several or even dozens of orders of magnitude, in order to enhance the stability of the neural network, a logarithmic transformation is performed on these cross-scale data.[19] In addition, the above input and output data also need to be standardized, and finally, 90% of the sample data set is formed as the training set and 10% as the test set.

(iii) DNN topology and training

The neural network topology structure contains the input layer, hidden layers, and the output layer. The input layer contains 11 nodes corresponding to the two temperature parameters, as well as the logarithm of the number densities of 9 chemical components. The hidden layers contain a 4-layer fully connected structure ($256 \times 512 \times 1024 \times 512$), using the ReLU activation function. The output layer contains 58 nodes that output the logarithms of different transport coefficients, including: non-equilibrium thermal conductivity (heavy particle translational–rotational thermal conductivity, electron thermal conductivity, internal thermal conductivity), viscosity coefficient, 9 self-diffusion coefficients and 45 binary diffusion coefficients.

DNN training employs the Adam optimizer with a learning rate fixed at 0.001. After 10^5 epochs, the MSE loss converges to 1×10^{-6}. Figure 4 illustrates the variations of the MAE and MSE loss with the epochs during the training process.

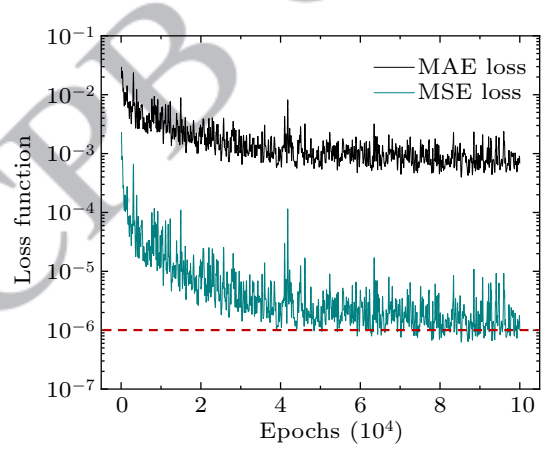


Fig. 4. Variations of the MAE and MSE loss with the epochs during the DNN training process.

3. Results

We use a utilitarian perspective to assess the performance of NeFlow-DNN: proving its accuracy, computational efficiency, and generalization. The computational program for the NeFlow-CE algorithm is used as a benchmark for comparison with the proposed NeFlow-DNN framework. NeFlow-CE originates from the combination of the physical property calculation program CE and the non-equilibrium flow field calculation program NeFlow. Among them, CE is a self-developed non-equilibrium physical property calculation program, and its implementation details can be found in our previous papers.[20,21] NeFlow is our self-developed non-equilibrium flow field program, and its implementation details are also described in our previous paper.[15]

The NeFlow-DNN coupling method, designed to accelerate non-equilibrium flow calculations, should be faster than the Chapman–Enskog method while maintaining high accuracy. Although the DNN in this paper has been trained on a specific vehicle's flow field, it must easily generalize to new flow simulations, such as different vehicle shapes, altitudes, and Mach numbers. In what follows, we first evaluate the performance of the DNN in predicting transport properties in an *a priori* manner. The DNN is then coupled with the non-equilibrium flow governing equations, and its accuracy in predicting flow fields and heat flux, as well as computational efficiency, is analyzed through comparison with the NeFlow-CE method. Finally, the predictive capability of NeFlow-DNN is further generalized to other flight shapes and flight conditions.

3.1. DNN *a priori* testing

First, the transport properties predicted by the DNN and Chapman–Enskog methods are compared to examine the performance of the DNN in an *a priori* manner. Figures 5(a)–5(f) present the full-field distributions of transport coefficients predicted by the DNN (including heavy particle translational–rotational thermal conductivity, electron thermal conductivity, internal thermal conductivity, viscosity coefficient, N_2–N_2 self-diffusion coefficient, and NO^+–e binary diffusion coefficient) using the steady-state flow field distribution of the ELECTRE vehicle at a flight altitude of 53.3 km and flight velocity of 4230 m/s as input. The results demonstrate that there is a minimal discrepancy between DNN predictions and target values. Figure 5(g) further displays the full-field average and maximum errors between the prediction and target for different transport properties across all 2501 grid points. For all the predicted transport properties, the average errors between the DNN and Chapman–Enskog method are below 0.5%, with the maximum errors occurring in internal thermal conductivity lower than 4%. This validates the accuracy of the DNN constructed in this study for transport property prediction.

CPB Online In Press

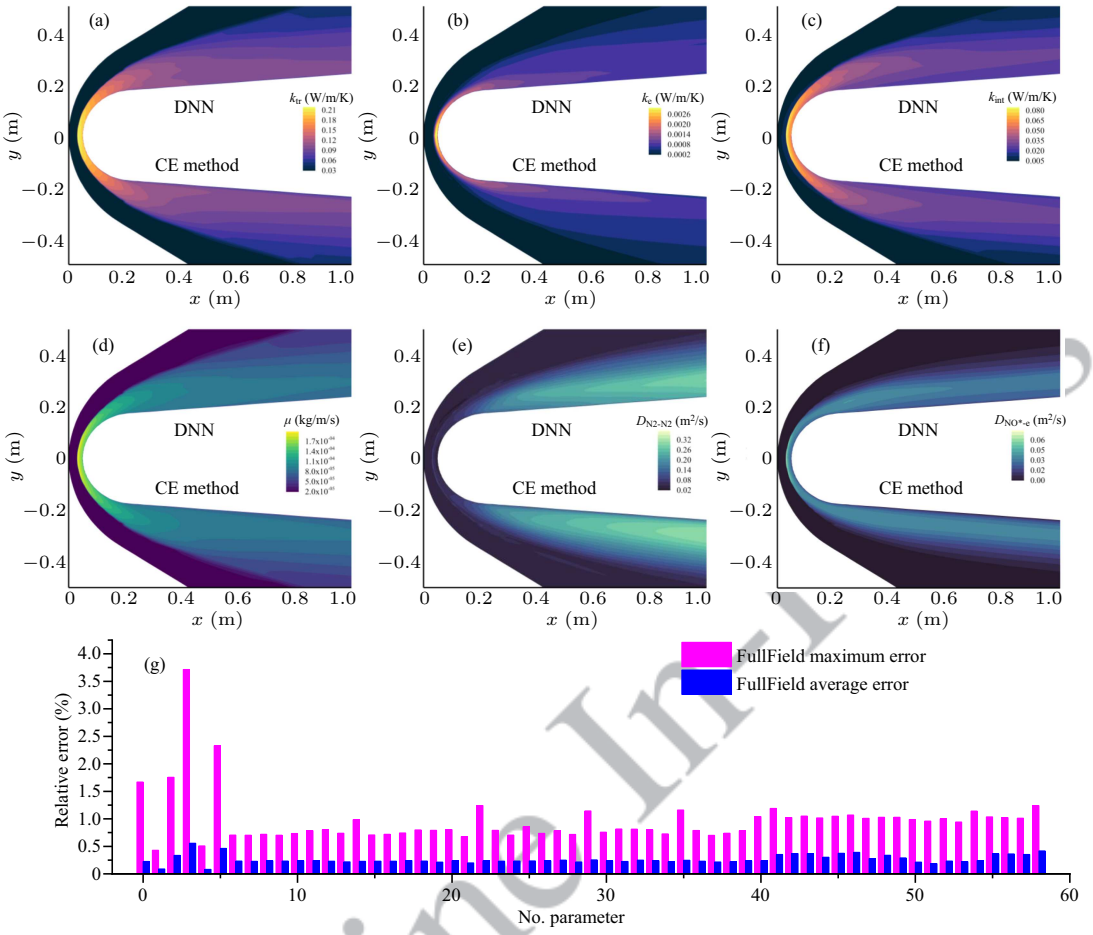


Fig. 5. Prediction of the distribution of transport coefficients by DNN and Chapman–Enskog methods (a)–(f), and the relative error (g).

3.2. NeFlow-DNN coupling results

Furthermore, we evaluate the prediction accuracy and computational efficiency of the NeFlow-DNN coupled acceleration methodology. Figure 6 presents the distributions of density, velocity, pressure, translational–rotational temperature of heavy particles, and number densities of oxygen molecules and atoms within the flow field computed by NeFlow-DNN and NeFlow-CE for the ELECTRE vehicle at a flight altitude of 53.3 km and velocity of 4230 m/s. As shown in Figs. 6(a)–6(c), NeFlow-DNN accurately predicts the shock compression effect of the high-speed incoming flow around the vehicle. The velocity sharply decreases within the shock layer, accompanied by abrupt increases in pressure and density. Furthermore, Fig. 6(d) reveals that the temperature within the shock layer rises significantly, reaching up to 8000 K. NeFlow-DNN precisely captures the conversion of kinetic energy to thermal energy within the shock layer and the subsequent energy transport processes. Under such extreme thermal conditions, molecular dissociation becomes prominent in the flow field. NeFlow-DNN also accurately predicts the chemical reactions and species diffusion processes occurring in the flow field. The distributions of flow parameters, thermal parameters, and chemical species computed by NeFlow-DNN and NeFlow-CE exhibit remarkable consistency. This robust agreement fully validates the capability of the NeFlow-DNN method to reliably and accurately characterize the parameter distributions within the flow field.

In addition to the flow field parameters, we are also concerned with the heat transfer and stress on the surface of the vehicle. Figure 7 presents the surface heat flux and pressure distribution of the ELECTRE vehicle calculated by NeFlow-DNN, NeFlow-CE, and Gupta–Yos/CCS models. It can be observed that the heat flux and pressure distributions predicted by NeFlow-DNN align closely with the computational results of NeFlow-CE, while also showing minimal deviation from experimental data. Meanwhile, comparing the DNN model with the Gupta–Yos/CCS model shows that the heat flux distribution predicted by the Gupta–Yos/CCS model is slightly higher, while the predicted pressure distributions by the two models are quite similar, because the pressure distribution is mainly determined by the shock structure and vehicle shape.

Figure 8 further compares the CPU computation time between NeFlow-DNN and NeFlow-CE. The results indicate that the computation time required for the NeFlow-DNN calculation is approximately 1/70-th of that for the NeFlow-CE method. This confirms that the NeFlow-DNN accelerated calculation method constructed in this study significantly enhances the computational efficiency of non-equilibrium flow simulations.

CPB Online In-Press

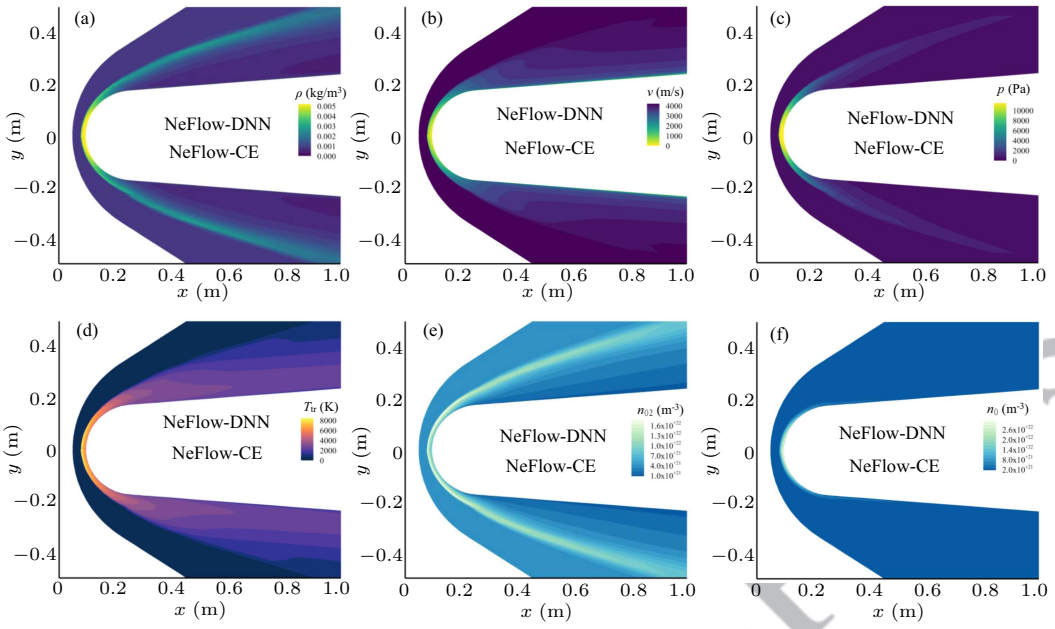


Fig. 6. Distributions of flow-field parameters calculated by NeFlow-DNN and NeFlow-CE for ELECTRE 53.3 km, 4230 m/s condition.

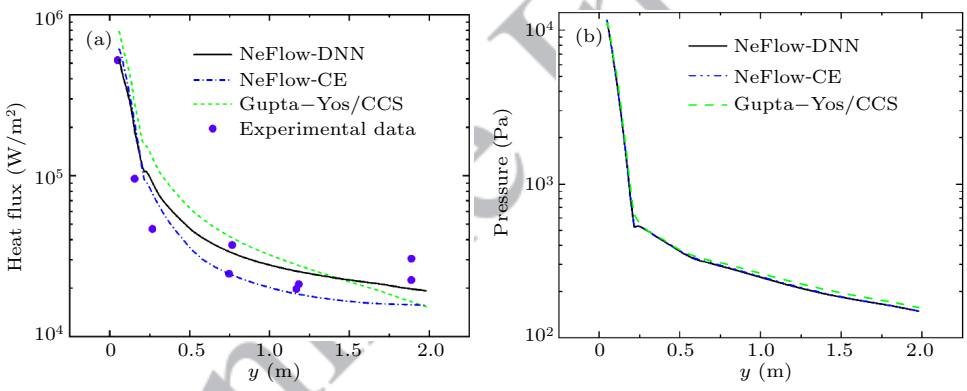


Fig. 7. (a) Wall heat flux and (b) pressure distribution calculated by NeFlow-DNN, NeFlow-CE, and Gupta–Yos/CCS models for ELECTRE, and compared with the experimental data.

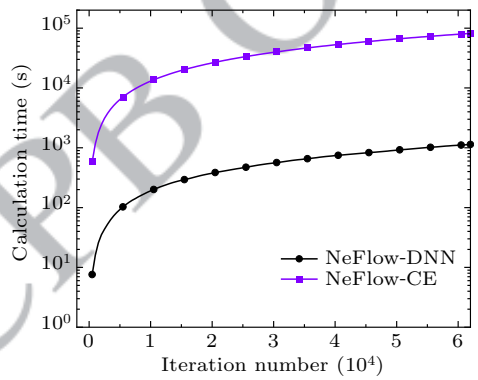


Fig. 8. CPU time cost comparison between NeFlow-DNN and NeFlow-CE for ELECTRE.

3.3. Generalization

In order to be useful, a learned model must accurately simulate flows outside of the training distribution. We hope that our model can generalize well because the DNN has learned the transport data under a wide range of non-equilibrium conditions. Therefore, it can be applied to flow simulations in more flight states. We consider two different types of generalization tests: (i) flow around a 90-mm-diameter cylinder with an inflow pressure of 687 Pa, temperature of 694 K, and velocity of 4776 m/s; (ii) flow around Japan's Titans vehicle, flying at a height of 88 km and speed of 6238 m/s.[22] As shown in Fig. 9, for the cylinder flow case, the flow field pressure and temperature distributions calculated by NeFlow-DNN and NeFlow-CE match extremely well. Both methods also accurately predict the vehicle surface pressure distribution. For the Titans flow case, as shown in Fig. 10, the density distribution and number density of N_2 calculated by NeFlow-DNN and NeFlow-CE are very close. Meanwhile, the local error distribution indicates that for the number density of N_2, the maximum error is 20%, mainly distributed at the shock wave area. However, in most of the flow field regions, the relative errors calculated by the two methods are lower than 4%. For the density field distribution, the maximum error is 15%, mainly located near the shock wave, and the relative error of the internal flow field within the shock wave is lower than 5%. This indicates that the NeFlow-DNN constructed in this work can be generalized to more vehicle shapes and flight conditions.

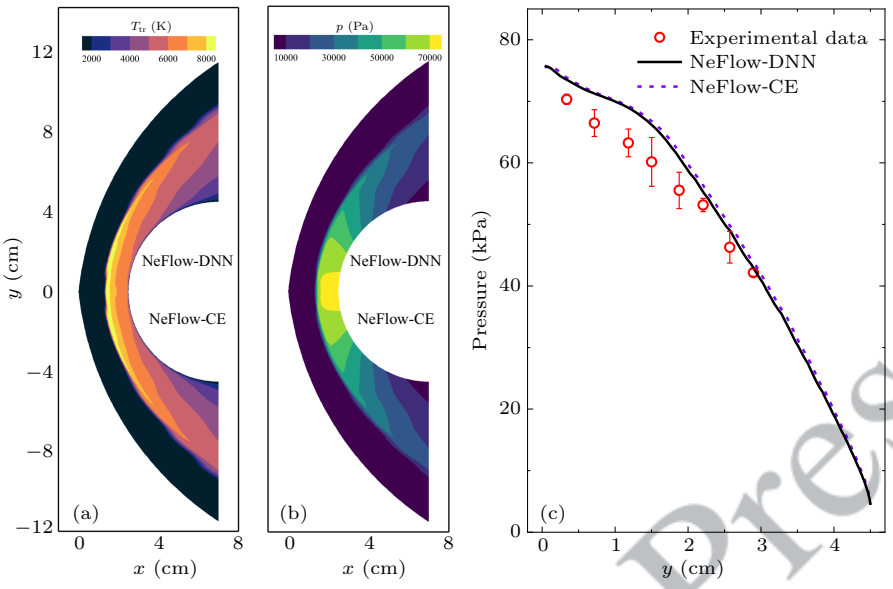


Fig. 9. Distributions of flow-field parameters and surface pressure calculated by NeFlow-DNN and NeFlow-CE for 90 mm-diameter cylinder.

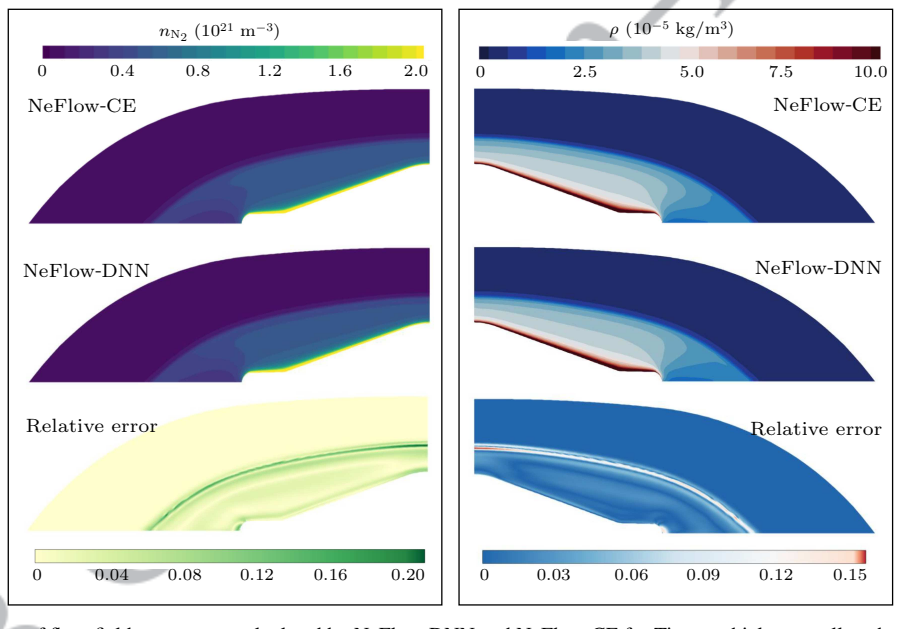


Fig. 10. Distributions of flow-field parameters calculated by NeFlow-DNN and NeFlow-CE for Titans vehicle, as well as the local relative error.

4. Discussion

In this work, we propose a data-driven approach for calculating transport properties and achieving acceleration in non-equilibrium flow computation. This method delivers high accuracy comparable to the conventional perturbative Chapman–Enskog method. By replacing complex interparticle potentials, collision integrals, and polynomial calculations with matrix operations in neural networks, it leverages machine learning to rapidly compute high-dimensional approximations of transport coefficients within the framework of discretized non-equilibrium flow equations. Ultimately, this approach achieves a 50–70× speedup in computational performance. The DNN training data originate from transport coefficients under extensive non-equilibrium conditions, enabling the method to demonstrate strong generalization capability across complex geometries and diverse flight conditions.

What prospects do our results suggest for accelerating complex non-equilibrium flows? In general, the computational cost T of efficient machine learning-augmented simulations for time-dependent PDEs scales as follows:

$$T \sim (C_{\text{eqs}} + C_{\text{phypro}} + C_{\text{chem}})^{N^{d+1}}, \tag{17}$$

where C_{eqs} is the cost of solving the discretized equations per grid point, C_{phypro} is the cost of calculating the physics properties (including the thermodynamics and transport coefficients) per grid point, C_{chem} is the cost of solving the chemical reactions and related mass/energy sources per grid point, N is the number of grid points along each dimension of the resolved grid, and d is the number of spatial dimensions. The stronger the real gas effects and non-equilibrium effects in the flow, the greater the proportion of the latter two terms. For the

high-speed, high-enthalpy flows studied in this work, where $(C_{\text{phypro}} + C_{\text{chem}})/C_{\text{eqs}} \approx 50$, we observed a reduction in computational cost by one to two orders of magnitude. For extension to three-dimensional and more complex problems, we anticipate a speedup ranging from 10^2 to 10^4.

In summary, our approach extends the Pareto frontier of efficient CFD simulations. By using machine learning to accelerate CFD, we demonstrate that, beyond optimizing equation discretization or solvers, computational efficiency gains are also attainable via accelerated computation of data-intensive terms (*e.g.*, transport properties, thermochemical reactions). We anticipate significant unexplored potential for these two strategies in ML-enhanced CFD, particularly for low-temperature plasmas, high-speed shock layer flows, and non-equilibrium combustion. This enables users to resolve computationally expensive non-equilibrium flow simulations faster or enhance accuracy without additional cost.

Acknowledgements

Project supported by the National Natural Science Foundation of China (Grant Nos. 12547156, 12375245, and 12535016) and the Fundamental Research Funds for the Central Universities (Grant No. YWF-23-L-1221).

References

[1] Gnoffo P A 1999 *Annu. Rev. Fluid Mech.* **31** 459
[2] Anderson J D 2006 *Hypersonic and High-Temperature Gas Dynamics*, 2nd edn. (American Institute of Aeronautics and Astronautics)
[3] Passiatore D, Sciacovelli L, Cinnella P and Pascazio G 2022 *J. Fluid Mech.* **941** A21
[4] Du Y W, Sun S R, Tan M J, Huang H J, Yan C, Meng X, Chen X and Wang H X 2023 *J. Fluid Mech.* **977** A39
[5] Palmer G E and Wright M J 2003 *J. Thermophys. Heat Transfer* **17** 232
[6] Chapman S and Cowling T G 1958 *Am. J. Phys*. **30**
[7] Du Y W, Sun S R, Tan M J, Zhou Y, Chen X, Meng X and Wang H X 2022 *Acta Astronaut.* **193** 521
[8] Sanderson S R, Hornung H G and Sturtevant B 2004 *J. Fluid Mech.* **516** 1
[9] Schramm J M, Hannemann K and Hornung H G 2023 *J. Fluid Mech.* **954** A32
[10] Wilke C R 1950 *J. Chem. Phys.* **18** 517
[11] Blottner F G, Johnson M and Ellis M 1971 *Tech. Rep.* SC-RR-70-754 NASA
[12] Gupta R N, Yos J M, Thompson R A and Lee K P 1990 *Tech. Rep.* RP-1232 NASA
[13] Hornung H G, Gollan R J and Jacobs P A 2022 *J. Fluid Mech.* **951** A6
[14] Devoto R S 1968 *J. Chem. Phys.* **2** 617
[15] He Q S, Sun S R, Cao X, Jia H, Du Y W and Wang H X 2023 *Aerosp. Sci. Technol.* **141** 108524
[16] Murphy A B 2012 *Chem. Phys.* **398** 64
[17] Capitelli M, Colonna G and Gorse C 2000 *Eur. Phys. J. D* **11** 279
[18] Ghorui S and Pfender E 2008 *Plasma Chem. Plasma Process.* **28** 553
[19] Zhang T H, Yi Y X, Xu Y F, Chen X Z, Zhang Y Y, E W N and Xu Z Q 2022 *Combust. Flame.* **245** 112319
[20] Wang H X, Sun S R and Chen S Q 2012 *Acta Phys. Sin.* **61** 195203 (in Chinese)
[21] Wang H X, Chen S Q and Chen X 2012 *J Phys. D: Appl. Phys.* **45** 165202
[22] Takahashi Y and Yamada K 2018 *Acta Astronaut.* **152** 437

CPB Online In Press